Title

Dissociate Lattice Oxygen Redox Reactions from Capacity and Voltage Drops of Battery Electrodes

Authors

Jinpeng Wu,[1,2,3] Zengqing Zhuo,[4,2] Xiaohui Rong,[5] Kehua Dai,[6,2] Zachary Lebens-Higgins,[7,2] Shawn Sallis,[8,2] Feng Pan[4], Louis F. J. Piper,[7] Gao Liu,[8] Yi-de Chuang,[2] Zahid Hussain,[2] Qinghao Li,[5*] Rong Zeng,[9*] Zhi-xun Shen,[1,3,10*] Wanli Yang[2*]

Affiliations

1. Geballe Laboratory for Advanced Materials, Stanford University, Stanford, California 94305, USA

2. Advanced Light Source, Lawrence Berkeley National Laboratory, Berkeley, California 94720, USA

3. Stanford Institute for Materials and Energy Sciences, SLAC National Accelerator Laboratory, Menlo Park, CA 94025, USA

4. School of Advanced Materials, Peking University Shenzhen Graduate School, Shenzhen 518055, China

5. Key Laboratory for New Energy Materials and Devices, Institute of Physics, Chinese Academy of Sciences, School of Physical Sciences, University of Chinese Academy of Sciences, Beijing 100190, China

6. School of Metallurgy, Northeastern University, Shenyang 110819, China

7. Department of Physics, Applied Physics and Astronomy, Binghamton University, Binghamton, New York 13902, USA

8. Environmental Energy Technologies Division, Lawrence Berkeley National Laboratory, Berkeley, California 94720, USA

9. Department of Electrical Engineering, Tsinghua University, Beijing 100084, China

10. Department of Physics and Applied Physics, Stanford University, Stanford, California 94305, USA

* Correspondence to (QL) lqh@iphy.ac.cn, (RZ) zengrong@tsinghua.edu.cn, (ZS) zxshen@stanford.edu, (WY) wlyang@lbl.gov

One-sentence Summary

Lattice oxygen redox is not responsible for the capacity and voltage decay in battery electrodes.

Abstract

The oxygen redox (OR) reaction is a promising concept for improving battery energy density, however, oxygen activities are generally

considered detrimental to the stability and kinetics of batteries. Studies of OR activities often mix the lattice OR with other oxygen-involved reactions, such as gas release, radical oxygen evolution and surface reactions, further shadowing the true property of the practically meaningful lattice OR activities. Here, based on high-efficiency mapping of resonant inelastic X-ray scattering (mRIXS) of both the transition-metals and oxygen, we distinguish and quantify the lattice OR activities in $Na_{0.6}[Li_{0.2}Mn_{0.8}]O_2$. Through the comparison with $Na_{2/3}[Mg_{1/3}Mn_{2/3}]O_2$ that also displays very strong lattice OR but distinct electrochemical stability, our results unambiguously show that the significant capacity drop in $Na_{0.6}[Li_{0.2}Mn_{0.8}]O_2$ stems from non-lattice-OR activities while lattice OR remains strong and stable. Furthermore, the quantified Mn redox reaction shows opposite trends in the two systems and significant increase upon cycling in $Na_{0.6}[Li_{0.2}Mn_{0.8}]O_2$, leading directly to a dramatically lowered discharge voltage. Our comparative study of the two strong lattice OR systems with distinct electrochemical stability suggests that lattice OR itself is not the ringleader of the stability issue as conventionally believed. Instead, other irreversible oxygen activities and the likely associated growth of cationic reactions lead to the capacity and voltage fade. Distinguishing lattice OR from other oxygen activities is critical for revealing the true property of oxygen redox reactions, something that has not been emphasized enough. Many intriguing findings and thoughts are triggered by this critical clarification. We argue that lattice OR and other oxygen activities should/could be treated separately to achieve viable OR-based electrodes for high-performance batteries.

MAIN TEXT

Introduction

The demand for high-performance energy storage in today's sustainable energy applications, especially electric vehicles and power grid, requires both conceptual breakthroughs and practical developments of batteries (*1*). Conventionally, only transition-metal (TM) redox in oxide cathodes are considered practical in positive electrodes, because oxygen activities trigger various stability and voltage limit issues in batteries (*2, 3*). Such a conceptual barrier has been complimented by recent scrutinies of oxygen activities, which suggest that it could be possible to utilize reversible lattice oxygen redox (OR) reactions to achieve high energy-density Li-ion and Na-ion batteries (*4-6*). However, technical challenges on practical employments of OR reactions remain formidable. While the employment of this concept relies on reversible OR reactions in the bulk lattice, hereafter called "*lattice OR*", electrochemically active oxygen often seems to display inherent irreversibility and sluggish kinetics, which trigger performance decays in both capacity and discharge voltages (*5, 7, 8*).

Although extensive studies and debates on OR activities in battery electrodes have been reported and reviewed (*5*), few has tried to distinguish the practically meaningful “lattice-OR” from other irreversible oxygen activities such as oxygen gas release, radical oxygen evolution, and associated surface reactions, which were reported in many literature especially for Li-rich materials(*9-17*). As illustrated in literatures for both Li- and Na- ion systems, these irreversible oxygen activities take place mostly on the electrode surface and are directly associated with the surface configuration through unclear mechanism (*10, 15, 16*). For clarity of discussions, hereafter, we call such irreversible oxygen-oxidation “*non-lattice OR*” in this work; however, we note that this designation is just for being consistent with previous literature. In reality, such oxygen activities involve only irreversible oxygen oxidation, which are not “red-ox” activities and should not be called oxygen “redox” at all.

So far, OR chemistry has been mostly studied and discussed without clear differentiation between lattice and non-lattice OR activities defined above. A common approach to access OR reactions is based on transition-metal measurements, because OR could be naturally invoked if the cationic redox reactions cannot compensate the electrochemical capacity. Although this is valid for evaluating the total OR activities, the results could only represent a mixed contribution from both (reversible) lattice OR and (irreversible) non-lattice OR (oxidation), so the true properties of the critical lattice OR reactions cannot be distinguished and disclosed. Endeavors trying to probe OR reactions more directly were mostly based on popular oxygen spectroscopy of O-*K* XPS and absorption, which encounter technical limitations on probe depth and entangled signals (*18*). Nonetheless, several works have attempted to disentangle the different activities in OR systems (*19-22*). It is clear through these efforts that the contributions from lattice and non-lattice OR activities are highly material dependent. Some systems display almost purely lattice OR, e.g., $Na_{2/3}Mg_{1/3}Mn_{2/3}O_2$ (NMMO) and $Na_{2/3}Mg_{0.28}Mn_{0.72}O_2$ (*22, 23*), while most other electrodes show significant amount of non-lattice oxygen involvements, e.g., Li-rich compounds (*9-14*). Due to the irreversible nature of the non-lattice OR, without differentiating the lattice OR from non-lattice OR activities, the critical question on how lattice OR affects the electrochemical performance remains elusive. However, the unique property of the NMMO material with almost purely lattice OR provides an excellent opportunity for a comparative study with another analog system with both lattice and non-lattice OR reactions, which inspires the detailed investigation of $Na_{0.6}[Li_{0.2}Mn_{0.8}]O_2$ (NLMO) in this work.

Technically, the lack of clarification of the lattice OR activities is largely due to the technical challenge on directly detecting and distinguishing lattice-OR contributions from the other non-lattice OR and cationic activities. Additionally, a reliable probe of lattice OR reactions requires direct and quantitative detections of both the cationic (TM *3d*) and

anionic (O *2p*) redox states in the bulk lattice. Such a technical challenge has been solved only recently through the developments of ultra-high efficiency mapping of resonant X-ray inelastic scattering (mRIXS) technique and data-analysis methodologies (*18, 22, 24*). For cationic redox reactions, mRIXS solves the TM-*L* distortion issue in conventional absorption spectroscopy through the inverse partial fluorescence yield (iPFY) with high enough energy resolution (*24*). Compared with hard X-ray TM-*K* absorption spectroscopy, mRIXS-iPFY is a direct detection of the TM-*3d* valence states with about 200 nm probe depth for most TM *L*-edges (*25*). The direct *3d* detection is sensitive enough for quantitative analysis of almost all the relevant TM oxidation states (*18, 26*). For reactions involving oxygen, mRIXS successfully fingerprints the lattice OR reactions through a specific feature at 523.7 eV emission energy(*18, 22, 27, 28*). The emission energy of this feature matches the spectroscopic signature of oxidized oxygen, which was found to be from excitations to unoccupied O *2p* states, i.e., non-divalent as O^{2-} has only fully occupied 2p states (*29*). The crucial achievement through O-*K* mRIXS is that this lattice OR feature is isolated from the broad TM-O hybridization features around 525 eV emission energy that are long known to the physics community(*30*). This difference in emission energy through mRIXS ultimately resolve the entangled signals in conventional soft X-ray absorption spectroscopy (sXAS) and distinguishes the lattice oxidized oxygen involved in lattice OR reactions (*18*). Furthermore, because mRIXS reveals the full spectroscopic profile of lattice OR reactions along both the excitation and emission energies, an intensity integration of the critical mRIXS feature through the super-partial fluorescence yield (sPFY) analysis could quantify the variation of oxidized oxygen in electrodes (*22*). Additionally, the irradiation effect has also been carefully checked and the oxidized oxygen mRIXS feature in battery electrodes could only be eliminated by high-flux radiation, which directly rules out the possibility of photon-induced mRIXS feature of oxidized oxygen(*31*). The mRIXS observation of the oxidized oxygen is thus intrinsic, and could at worst be underestimated if the beam flux is not carefully controlled (see "Materials and Methods"). Therefore, these recent technical and methodological developments and demonstrations have established the combined TM-*L* mRIXS-iPFY and O-*K* mRIXS-sPFY analysis as so far the most direct and quantitative probes of both cationic and anionic redox states in batteries(*18, 22, 27, 28*).

mRIXS-based quantifications of the lattice OR activities in NMMO and Li-rich $Li_{1.17}Ni_{0.21}Co_{0.08}Mn_{0.54}O_2$ compounds have shown an intriguing phenomenon: lattice OR could display high reversibility in electrode systems with or without other non-lattice oxygen activities (*22*). Because non-lattice OR reactions, e.g., gas release and surface reactions of radical oxygen, are irreversible, such a finding questions our common understanding of OR effects on electrochemistry, and it becomes vital and practically meaningful to clarify whether lattice OR is associated with the electrochemical decay. Such a clarification could be

achieved through detailed and quantitative comparison between NMMO and another analog system, NLMO here, both with strong OR reactions, but with distinct electrochemical decays in the capacity and discharge voltage.

In this work, we quantitatively analyze both the lattice OR and Mn redox in $Na_{0.6}[Li_{0.2}Mn_{0.8}]O_2$ (NLMO) with the focus on clarifying the effects of oxygen activities on electrochemistry. NLMO involves only one cationic (Mn) and one anionic (O) possible charge transfer site, therefore, could be directly compared with NMMO. Contrasting the NMMO system that displays a relatively stable electrochemical (*22*), NLMO system shows dramatic capacity fade and a fast-growing discharge plateau at a low voltage in only 12 cycles (Fig. 1). Because both NMMO and NLMO display strong lattice OR reactions, such a clear electrochemical contrast provides direct evidence to decouple the lattice OR from the capacity and voltage decay. Through Mn-*L* mRIXS-iPFY and O-*K* mRIXS-sPFY quantifications, both the lattice OR and bulk Mn redox contributions to electrochemistry are quantified in NLMO. Our experimental results reveal a surprisingly high reversibility (97%) of the lattice OR during the initial cycle of NLMO, resembling that in NMMO. However, a large amount (34%) of the oxygen oxidation during the initial charge are found due to the irreversible non-lattice OR, which contrasts NMMO and is responsible for the capacity loss in general. Additionally, bulk Mn redox starts to emerge from the initial discharge and grows significantly upon cycling, with Mn-capacity contribution almost doubled within only 12 cycles, again contrasting the relatively stable Mn redox contribution in NMMO after 100 cycles. The growing Mn redox corresponds to the development of lower-voltage discharge plateau in NLMO system. Our results unambiguously show that capacity and voltage drops are not inherent problems of lattice OR activities. Instead, the majority of the capacity decay in OR systems is due to non-lattice OR reactions, while the growing cationic redox upon cycling is responsible for the low-voltage plateau during discharge. This critical clarification triggers many intriguing questions for future researches and developments.

Results

Materials and electrochemistry. The P3-type $Na_{0.6}[Li_{0.2}Mn_{0.8}]O_2$ is synthesized by a solid-state reaction as reported previously (*32*). The electrochemical performance has been extensively studied as shown in Fig. S1. The structure of the material was studied by XRD (Fig. S2). The morphology of the particles studied by SEM (Fig. S3) shows that the particles are of the size less than 7 μm (*32*). Compared with P2-type NMMO, the NLMO studied here is of the different P3-type stacking sequence (Fig. 1) (*32*-*35*). Otherwise, the major difference between the two systems is only on the dopants in the TM-O layer, i.e., Li in NLMO and Mg in NMMO. This work focuses on ten representative NLMO samples with different states of charge (SOC) from 1, 2, and 12 cycles, as marked in Fig. 1A. Samples are named as (cycle-number)C/D(voltage

value), with “C” and “D” corresponding to charging and discharging processes, respectively, e.g., 1C4.5 represents an electrode after the 1st cycle (1) charging (“C”) to 4.5 V (4.5) voltage.

Previous studies have reached the agreement that significant amount of OR activities are involved in the cycling of both NMMO and NLMO systems due to the nominal high-valence Mn^{4+} in pristine materials due to Li/Mg doping (*33*-*36*). However, as shown in Fig. 1, the NMMO and NLMO display very different electrochemical profile. The NLMO electrodes display a significant capacity drop and a growing low-voltage discharge plateau within only tens of cycles, providing a unique system to study these electrochemical performance decay in a OR dominating system.

Quantification of bulk Mn redox through mRIXS-iPFY. As reviewed before (*25, 26*), sXAS of TM-*L* edges provide the most direct and quantitative detections of the TM-*3d* valence states. For Mn, absolute values of valence distributions at different electrochemical states can be directly quantified through a straightforward linear combination fitting of the $Mn^{2+/3+/4+}$ reference spectra (*37*). Unfortunately, although sXAS could typically be collected in both total electron yield (TEY) and total fluorescence yield (TFY) modes with probe depth of 10 and 100 nm, respectively (*38*), Mn-*L* sXAS in the bulk-sensitive TFY mode encounters serious lineshape distortions due to the significant signal contributions from oxygen in the samples (*24, 39*), hindering reliable quantifications. As shown in Fig. S4, Mn-*L* TFY spectra are seriously distorted and cannot be used for quantifying the bulk Mn redox reactions. Therefore, we employ Mn-*L* mRIXS-iPFY to probe the bulk Mn valence states. The principle of iPFY through energy-resolved fluorescence signals has been explained by Achkar *et al*. through Silicon drift detectors, and has been demonstrated to be a non-distorted bulk-sensitive probe of TM-*L* edges (*39*). Here, we extract Mn-*L* iPFY signals from mRIXS (Fig. 2) by integrating the florescence signals from oxygen with emission energy range of 475-525 eV (Fig. 2B). We note that the energy resolution of our mRIXS results are several hundred times higher than silicon drift detectors in previous iPFY studies, leading to a clear separation between the emission signals from O (around 520 eV emission energy) and Mn (around 640 eV emission energy) for extracting clean iPFY spectra (*18, 24*).

Fig. 2A shows the iPFY Mn-*L* spectra (solid lines) of the representative NLMO electrodes at different electrochemical states at each cycle. mRIXS images and mRIXS-iPFY spectra of all the electrodes are presented in Fig. S5 and Fig. S6, respectively. The non-distorted Mn-*L* iPFY enables quantitative analysis of the Mn valence states in the bulk at different electrochemical states through the established linear combination fitting based on the Mn reference spectra (*40*). The fitting ones (dotted lines in Fig. 2A) completely overlap with our experimental

iPFY data (solid lines in Fig. 2A), indicating a precise quantification of the Mn oxidation states with the values summarized in Table 1.

In general, Mn^{4+} dominates the bulk signal of most electrodes studied here, which is expected by considering the NLMO stoichiometry with only nominal Mn^{4+} in pristine materials. However, a weak but clear variation around 641.5 eV at different electrochemical states, with the intensity growing upon cycling, indicates a finite amount of Mn^{3+} developed in the system. Such an evolution of Mn states is clearly revealed through the quantification analysis (Table 1) that is visualized in Fig. 2C.

The tiny capacity before the initial charge plateau corresponds to a small drop (increase) of Mn^{3+} (Mn^{4+}) contents (Table 1), indicating a trace amount of Mn^{3+} exists in the pristine material from sample preparation and is oxidized to Mn^{4+} at the beginning of the 1^{st} charge. Throughout the long charge (4.25 V) and discharge (4.0 V) plateau, the Mn remains Mn^{4+}. However, Mn^{3+} starts to emerge below 3.95 V during discharge with a decreasing amount of Mn^{4+}, revealing that $Mn^{3+/4+}$ redox reactions contribute to the short low-voltage discharge plateau around 3.8 V. More importantly, upon electrochemical cycling, the quantified contributions from $Mn^{3+/4+}$ redox reactions continuously increase upon cycling and the average Mn valence state drops significantly with 15% Mn^{3+} in discharged electrode after only 12 cycles (Table 1, Fig. 2C).

Therefore, our quantitative analysis based on Mn-*L* mRIXS-iPFY clearly reveals the evolving $Mn^{3+/4+}$ redox in the bulk upon electrochemical operations: i) $Mn^{3+/4+}$ redox emerges from the first discharge cycle. ii) Contributions from Mn redox grow upon cycle numbers. iii) The overall Mn valence states drop significantly in NLMO after only 12 cycles. The quantified oxidation states of Mn directly correspond with the electron charge numbers, and the electrochemical capacity associated with Mn redox can be calculated based on Nernst Equation, as provided in Table 1. It is clear that the quantified Mn redox contribution matches the electrochemical capacity during the discharge 3.8 V plateau, leading to a continuous voltage drop upon cycling.

More importantly, such a dramatic development of Mn redox with only 12 cycles is in sharp contrast with the NMMO system, where Mn redox contributions to electrochemistry remain the same level after a hundred cycles (*22*).

Surface and Irreversible Reactions in NLMO. Another critical finding, based on Mn-*L* quantifications, is from the surface-sensitive sXAS-TEY signal. As shown in Fig. 2A and Fig. S4, surface TEY contrasts bulk mRIXS-iPFY spectra with a clear signature of Mn^{2+}, which could be directly seen in the raw data of Mn-*L* sXAS plots through the low-energy peak at about 640 eV. On the one hand, the sharp contrast between the

surface-sensitive TEY and mRIXS-iPFY indicates that the signals of mRIXS-iPFY are indeed dominated by the bulk information. On the other hand, these surface-sensitive TEY spectra could also be precisely fitted through linear combinations of the references (*26, 37, 40*), with the values given in Table 1 and visualized in Fig. 2C.

Strikingly, during the charge (oxidation) process, the low-valence Mn^{2+} content increases significantly on surface and reaches the maximum value at the fully charged state (Table 1 and Fig. 2C). Such a counterintuitive behavior of the enhancing surface Mn^{2+} during charge has been found in high-voltage Li-ion battery electrodes, suggesting significant surface reactions taking place during the high-potential charge involving electrolyte degradation (*41*). It is important to note that, although surface Mn^{2+} development could be seen in Na-ion battery electrodes (*22, 37*), the activity typically follows the expected reduction process during discharge. In direct contrast, NMMO displays an enhanced Mn^{2+} concentration during discharge as expected (*22*). Therefore, the reversed behavior of surface Mn^{2+} upon SOCs in NLMO is a clear signature of strong surface reactions. For systems involving electrochemically activated oxygen, such a surface behavior resembles the typical Li-rich compounds that often displays surface condensation and TM reduction after high-voltage charging because of both the oxygen release and surface reactions involving electrolyte(*10-14, 17*).

The oxygen release and surface reactions have been extensively studied in Li-rich layered compounds, although many questions remain open (*10-14*). In general, it is believed that, during the high voltage charging, many different types of side reactions could take place on the electrode surface, including the decomposition of the electrolyte itself and the surface carbonates. Additionally, oxygen could be released from the electrode materials, in the form of either O_2 gas or radical oxygen, $^{\cdot}O_2$, which is highly reactive with the electrolyte on the electrode surface (*11, 17*). These studies have also shown that TM reduction is directly associated with these side reactions (*11*).

Indeed, a very recent work by Bruce *et al*. on gas release studies shows that the NLMO system shows O_2 gas release and radical O evolution at very high voltage, contrasting the relatively stable NMMO system (*15*). Their work also suggests that both of the oxygen release and radical oxygen evolution take place on the surface within about 10 *nm* of depth. The contrasting surface Mn^{2+} behaviors in NLMO and NMMO systems described in this work are generally consistent with the gas release findings, because oxygen release will lead to the reduction of TMs especially in the surface regime (*11*). Therefore, the counterintuitively enhanced surface Mn^{2+} signals in the charged state of NLMO indicates that the irreversible non-lattice oxygen redox, which takes place mostly in the surface regime in the forms of oxygen release and surface reactions, is much stronger compared with NMMO. We note

that such a conclusion is directly supported by our lattice O redox quantification results below.

Quantification of Lattice O redox through mRIXS-sPFY. The quantifications of Mn redox reactions suggest that Mn redox contributes to only a very limited amount of electrochemical capacity. This is expected as NLMO should be a strong OR system due to the high-valence Mn in its pristine state. However, although the OR reactions are supposed to dominate the electrochemical cycling, pre-edge features of O-*K* sXAS display only a small change at different electrochemical states in both TEY and TFY modes (Fig. S7). As a matter of fact, we have recently clarified that the variation of the O-*K* sXAS pre-edges is dominated by the changes of TM-O hybridization, not OR reactions (*18*). Therefore, as introduced earlier, O-*K* mRIXS is capable of isolating the lattice OR signature from the strong hybridization features and is thus employed here to detect and quantify the lattice OR reactions through previously demonstrated methodologies (*18, 22, 27, 42*).

Fig. 3 displays the mRIXS and sPFY results of all the representative NLMO electrodes at different cycling states, with samples indicated in Fig. 1. It is clear that the signature of the oxidized oxygen at 523.7 eV emission and 531 eV excitation energies emerges with the 4.25 V charge plateau, and disappears after the 4 V discharge plateau (red arrows in Fig. 3A). This defines a voltage boundary of lattice OR reactions, and is consistent with the aforementioned analysis on Mn redox reactions, which display Mn-*L* spectroscopic variations only outside the OR voltage range (Table 1, Fig. 2C). Therefore, unlike most Li-ion compounds, e.g., Li-rich electrodes, where TM and O redox are often mixed together during discharge (*19, 27*), the cationic and anionic redox reactions in NLMO takes place at different potential ranges, the same as NMMO system (*22*). An interesting question is whether the separated (mixed) redox reactions are somehow more inherent to Na-ion (Li-ion) electrodes, which deserves further studies of other electrode materials. Nonetheless, the mRIXS results of O-*K* and Mn-*L* set an electrochemical boundary of the two redox reactions, which will be used later as one of the ways for quantifying the lattice OR contributions to the electrochemical capacity.

Compared with O-*K* sXAS and/or individual RIXS cuts, an mRIXS image is able to detect the full profile of the oxidized oxygen along both the excitation and emission energy energies (*29*), providing a unique opportunity to quantify the complete spectroscopic intensity of the oxidized oxygen states. Fig. 3B and 3C display the sPFY extracted by integrating the intensity within the characteristic emission-energy window around 523.7 eV (signals between the two dotted lines marked on Fig. 3A). In this way, the specific oxygen redox mRIXS feature is reduced to a 1D sPFY spectrum. The corresponding intensity around 531 eV excitation energy varies with electrochemical states (Fig. 3B), with a peak and dip clearly shown in charged and discharged states

(Fig. 3C). The full intensity of oxidized oxygen feature could then be quantified by a simple area integration of the mRIXS-sPFY within 530-532 eV energy (see “Materials and Methods”).

The quantified mRIXS-sPFY intensities at different SOCs are presented in Table 2 and plotted in Fig. 4A on top of the electrochemical profile. First, it is clear that strong lattice OR reactions take place during the long charge and discharge plateaus. Mn redox, colored as blue, was quantified independently above (Table 1, Fig. 2C) and dominates the capacity outside these two high-voltage plateaus. Second, the mRIXS-sPFY peak area changes during initial charge (0.232) and discharge (0.224) suggests a highly (97%) reversible lattice OR reactions during the initial cycle, even higher than that in NMMO (79%) (*22*). Third, contrasting the highly reversible lattice OR reaction during the initial cycle, the electrochemical profile shows a significant capacity drop of the overall OR plateaus from charging (105.1 mAh/g) to discharging (66.6 mAh/g). This sharp contrast indicates that the strong lattice OR reactions and the loss of capacity are not strongly associated. Additionally, this also implies that a large portion of the overall OR contributions is not from lattice OR, which is consistent with the strong surface activities during charging. We therefore pursue a more detailed analysis to differentiate the lattice OR from other non-lattice OR contributions.

A relationship between the electrochemical capacity and the mRIXS-sPFY peak area change is needed to quantify the lattice OR capacity. Because studies show that the majority of non-lattice OR reactions take place during the charging process (*10*-*14*), the O-*K* sPFY peak-area change during discharge is therefore a more reliable probe of lattice OR. We first assume and test a proportional relationship between the sPFY peak-area change during discharge to the amount of lattice OR reactions. Such a simple dependence has been verified by the perfect match between electrochemical profile and sPFY peak area change in NMMO with pure lattice OR reactions (*22*). For NLMO, we test the validity of this linear dependence with the 1^{st}, 2^{nd}, and 12^{th} discharging processes, which display discharge capacities of 66.6, 59.5, and 39.7 mAh/g with the sPFY peak area changes of 0.224, 0.195, and 0.130, respectively. Therefore, the three tested discharge cycles consistently show a ratio between lattice OR capacity and sPFY peak area change, i.e., 303, 305, and 305 mAh/g per peak-area change during the 1^{st}, 2^{nd}, and 12^{th} discharge. Considering the slight broadening of spectroscopic features upon cycling from structural amorphization, these values are highly consistent, confirming that discharge capacity is indeed dominated by lattice OR with a quantification ratio of about 303 mAh/g per peak area change. Based on this self-consistent analysis and the conversion ratio, the quantified capacity from the lattice OR contribution at each discharge cycle is provided in Table 2, and visualized in Fig. 4B as the “mRIXS” results (narrow bars).

Discussions

Joint quantification results of Mn and O redox reactions. Based on the Mn-*L* mRIXS-iPFY and O-K mRIXS-sPFY results, we have now achieved two sets of quantified capacity from the Mn and O redox in NLMO. i) The Mn (Fig. 2C) and O (Fig. 4A) spectroscopic changes set the boundary between the cationic and anionic redox reactions, so electrochemical capacities can now be defined to specific redox reactions (Method-I). The values are plotted in Fig. 4B as framed wide columns from "electrochemistry". ii) The absolute values of electron charge transfer, as well as the capacity, from Mn redox can be calculated purely based on the Mn oxidation states quantified through Mn-*L* mRIXS-iPFY (Table 1). For OR contributions, the capacity could also be calculated based on the O-*K* sPFY peak area changes and the conversion ratio of 303 mAh/g per peak-area change, as detailed above (Method-II). The independently quantified Mn and lattice OR capacities from spectroscopy are also plotted in Fig. 4B as "mRIXS" results beside the electrochemistry results.

Low-voltage plateau with growing Mn redox. Fig. 4B visualizes the quantification results of Mn and lattice-O redox during the discharging process based on the two different methods. It is obvious that the quantifications from electrochemistry (Method-I) are in great agreement with the values from mRIXS-iPFY (for Mn redox) and mRIXS-sPFY (for lattice OR) results (Method-II). Additionally, Fig. 4B shows that, after only 12 cycles, the lattice OR capacity drops; however, the Mn redox contribution almost doubles. Note the $Mn^{3+/4+}$ redox contributions from Method-II are absolute values of electron charge transfer numbers purely based on spectroscopic results (Table 1). Therefore, the match between the Mn redox contributions from Method-II (purely spectroscopy) and the capacities of the low-voltage discharge plateau concludes that the growing low-voltage plateau during discharge is due to the continuously increasing $Mn^{3+/4+}$ redox upon cycling.

Very recently, the increasing cationic redox in Li-rich compounds was proposed as the central mechanism of voltage fade of Li-rich electrodes (*7*). Here, the NLMO shows a much clearer low-voltage reaction that grows upon cycling, and our quantification results experimentally conclude that this growing low-voltage reaction is due to $Mn^{3+/4+}$ redox reactions developed upon cycling of this Na-ion system. More importantly, contrasting these NLMO findings, the Mn redox capacities remain stable even after 100 cycles in NMMO, which also displays strong lattice OR reactions (*22*). Therefore, the contrast on the stability of Mn redox and the discharge voltage are not due to the strong lattice OR activities that exist in both NLMO and NMMO systems.

Capacity loss with non-lattice OR. While the discharge capacity could be well understood through the mRIXS quantifications of Mn and lattice OR reactions (Fig. 4B), the charging capacity significantly deviates from the mRIXS quantifications (Fig. 4C). This is consistent

with the strong surface reactions on NLMO as discussed above. In general, oxygen evolves from the NLMO during high-voltage charging in the form of gas release and/or radical oxygen, leading to irreversible surface reactions with CO_2 gas release (*15*). Such non-lattice OR activities are highly irreversible, i.e., they behave very differently from the reversible lattice OR detected in our mRIXS experiments. The quantitative comparison between the electrochemical capacity defined by method-I and the mRIXS quantifications through method-II shows that about 36.1 mAh/g capacity is from irreversible non-lattice OR contributions during initial charge (Fig. 4C). In addition to the capacity plots here, the quantification results in electron charge transfer numbers is provided in Fig. S8.

A striking finding emerges from the quantitative analysis of the charging process (Fig. 4C). With the lattice OR reactions being highly reversible (69 and 66.6 mAh/g during initial charge and discharge), the irreversible non-lattice OR activities almost fully cover the capacity loss. For example, the initial-cycle OR capacity loss is 105.1 (charge) – 66.6 (discharge) = 38.5 mAh/g (Fig. 4 B & C), or 0.131 (0.358 – 0.227) electron charge transfer (Fig. S8). This loss of capacity is dominated by the non-lattice OR contribution (36.1 mAh/g), plus only a very small (2.4 mAh/g) decay of lattice-OR contribution. The loss of OR capacity is compensated by the emerging Mn redox (8.9 mAh/g) during discharge, leading to the eventual value of 75.5 mAh/g discharge capacity. Such a capacity loss from non-lattice OR continues in the following cycles, i.e., non-Lattice OR capacity (12.6 mAh/g) gets totally lost while lattice OR maintain a decent reversibility during the 2^{nd} cycle (60.4 mAh/g charged, 58.0 mAh/g discharged, Fig. 4B, C). Therefore, the capacity loss of NLMO are from three contributions: i) the irreversible non-lattice OR dominates the loss of capacity; ii) lattice OR capacity drops only slightly, less than 5%; iii) the loss from OR is compensated by the emerging Mn redox, however, the Mn redox contribution remains much lower than the lost non-lattice OR capacity, leading to the drop of the total capacity.

The conclusion that capacity loss in NLMO is mainly from non-lattice OR reactions is again consistent with the contrast between NLMO and NMMO (Fig. 1). While both systems display strong lattice OR reactions, the significant capacity loss takes place only in NLMO with significant amount of non-lattice OR activities. Because only the reversible lattice OR reaction dominates the cycling in NMMO (*15, 22, 23*), no significant capacity drop is observed within 12 cycles.

Intriguing relationships and perspectives. This comparative study concludes that the significant capacity loss of NLMO is not from lattice OR reactions, and the low-voltage discharge plateau is from the growing cationic (Mn) redox upon cycling, several complex and intriguing relationships emerge from the observations here, which are critical for future studies and material optimizations.

Firstly, on the voltage fade, compared with NMMO system with strong lattice OR but stable Mn redox capacity for a hundred cycles (*22*), the NLMO here shows significant increase of Mn redox contributions for only 12 cycles. Although both systems display strong lattice OR reactions, NMMO shows almost purely lattice OR while NLMO features a large amount of non-lattice OR reactions during charging (*15, 23*). This indicates that the increasing Mn redox upon cycling is associated with non-lattice OR reactions, as also suggested for Li-rich compounds very recently (*7*). Secondly, even for NMMO system, voltage fade is observed, most clearly after 50 cycles and was attributed to the decrease of averaged Mn oxidation states (*22*). However, an interesting coincident is that the most significant decrease of lattice OR also takes place after 50 cycles there. This not only confirms that lattice OR itself is not responsible for the dropping discharge voltage; on the contrary, decreasing lattice OR reactions may be associated with part of the voltage drop, i.e., lattice OR should be stabilized, not suppressed, to maintain discharge voltage.

Thirdly, the practicability of the concept of lattice OR depends on how reversible and stable the reaction could be. Aside from the high reversibility of lattice OR during the initial cycle, the reaction displays a poor cyclability in only 12 cycles with capacity dropping from 66.6 to 38.7 mAh/g based on mRIXS quantifications (Fig. 4B). A close inspection shows that the loss of lattice OR capacity, corresponding to the decreasing difference of the mRIXS-sPFY peak-area between the charged and discharged states (Double arrows in Fig. 3C), is mostly from the discharged states. The sPFY remains roughly stable in the charged sates (Table 2, Fig. 3C); however, the sPFY of discharged states is obviously enhanced around 531 eV after only 12 cycles. This could be seen directly through the sPFY spectra in Fig. 3C, which shows that the intensity between 530-532 eV is clearly enhanced in the 12^{th} discharged state (green arrow in Fig. 3C), leading to the decrease of sPFY contrast between the charged and discharged states. Such a change of discharged states on lattice OR has also been seen in NMMO, however, the effect there is weak and spectroscopic lineshape broadening upon cycling cannot be ruled out (*22*). In NLMO, the change of sPFY intensity in discharged states is strong and cannot be simply interpreted by spectroscopic broadening upon cycling, i.e., discharged 12D3.5 displays dedicated signals around 531 eV (green arrow) that cannot be from peak broadening (Fig. 3C). Therefore, the sPFY here implies that the poor cyclability of lattice OR in NLMO is likely because the oxidized oxygen is not completely reduced back to O^{2-} in discharged states after extended cycles. This finding is in sharp contrast to our common belief that most reversibility and cyclability issues are associated with high-voltage charging. In the meantime, such irreversibility at discharged states could be associated with the increasing Mn redox activities upon cycling in NLMO (Fig. 2 & 4). Fundamentally, a reshuffling of the Mn and O electronic states is necessary to allow Mn redox to take place with the continued existence of non-divalent oxygen, which interestingly

assembles the situation in Li-rich materials, where cationic redox overlaps with OR reactions in a wide potential range during discharge (*27*).

Fourthly, the initial-cycle reversibility of lattice OR is much higher in NLMO (97%) than that in NMMO (79%) (*22*). Two differences between the systems may be associated with this initial reversibility. One unlikely scenario is that the significant amount of non-lattice oxygen activities in NLMO may have changed the redox-active oxygen configurations, as speculated above, and counterintuitively optimized the stability of lattice OR. The other likely effect is the Li dopants in NLMO, instead of the Mg in NMMO. Although both Li and Mg are electrochemically inactive, the comparisons with NMMO in this work have revealed that replacing Mg with Li changes all the three types of redox activities in NLMO: the non-lattice OR (significant in NLMO), lattice OR (better reversibility in NLMO), and Mn redox (growing upon cycling in NLMO) reactions. The quantifications of the redox processes here, not only contribute to further understandings the effect of Li and Mn dopants; but also, the results show directly that dopants of electrochemically inactive elements could change strongly the redox related activities in batteries.

To fully understand the many intriguing findings here is in dire need of the fundamental clarifications of the true driving force for activating oxygen in TM oxide electrodes towards different redox activities, which remains a grand challenge for future experimental and theoretical studies. We also note that other important questions remain unanswered, such as the relationship between lattice OR and surface properties (*9*) and the kinetics that leads to the strong hysteresis in NMMO (*5, 43*). Nonetheless, the key experimental conclusions of this work on the capacity and voltage drop make important corrections to our conventional wisdom. Our central results show that lattice OR itself is not responsible for the performance decay, and the real ringleaders are other irreversible oxygen activities. This means that it is critical to distinguish lattice OR from other oxygen activities for clarifying the concept of OR-based electrodes. The comparison between the two materials, NLMO and NMMO, implies that different types of OR reactions are intrinsic material properties, not simply the voltage range. This is another critical information that deserves future works on more systems to confirm and to clarify. Practically, the conclusions of this work lead to different aspects on material optimizations: lattice OR should/could be enhanced and maintained to be stable, e.g., through lattice doping, but other oxygen activities should/could be suppressed, e.g., through surface treatments. The combination of the two approaches holds the promise towards viable OR-based high-performance electrodes.

Materials and Methods

Material synthesis and electrochemical test. The P3-type $Na_{0.6}[Li_{0.2}Mn_{0.8}]O_2$ electrode material was synthesized by a solid-state reaction using precursor of Na_2CO_3 (99.9%, Alfa), LiOH (98%, Alfa), and MnO_2 (99.9%, Alfa). The prepared electrode material was assembled into CR2032 coin cells containing a metallic-Na anode, a glass-fiber separator, a liquid electrolyte of 1M $NaClO_4$ in ethylene, dimethyl carbonate (DMC), propylene carbonate (1:1:1 in volume), and fluoroethylene carbonate (2% in volume, for improving the high voltage cycle performance due to the higher redox potential than PC). The electrochemical test was carried out using Land CT2001A battery test system, in a voltage range of 3.5 - 4.5V at the rate of 0.1C (10 mAh g^{-1}) under room temperature. More details on materials and structural characterizations were reported previously (*32*).

Soft X-ray absorption spectroscopy (sXAS) and sample handling: sXAS measurement was performed in the iRIXS endstation at Beamline 8.0.1 of the Advanced Light Source (ALS) at Lawrence Berkeley National Laboratory (LBNL) (*24*). The electrode samples were cut into small pieces (about 3mm×3mm) in the Ar glove box, and pasted onto a sample holder. The sample holder was then loaded into a specially-designed sample transfer mini-chamber. The mini-chamber was then sealed, and mounted onto the iRIXS endstation under vacuum for direct pump-down to avoid any air exposure. All the TEY and TFY spectra were normalized to the beam flux measured by the upstream gold mesh. The resolution of the excitation energy is 0.15 eV without considering core-hole lifetime broadening. Refer to the previously published work with detailed procedures (*44*).

Mapping of resonant inelastic X-ray scattering (mRIXS). mRIXS was measured in the iRIXS endstation at Beamline 8.0.1 of ALS (*24*). The beam spot size is about 25*100 μm (*32*). Additionally, in order to increase the sampling across a large area of the electrode and to reduce the radiation damage effect, data were collected with controlled flux and itinerary samples throughout the measurements. Therefore, the mRIXS signals represent the overall information of a large amount of electrode materials. Considering the particle size of less than 7 μm, the area of mRIXS data collection covers thousands of particles. Mapping data were collected by the ultra-high efficiency modular spectrometer (*45*), with an excitation energy step of 0.2eV. The resolution of the excitation energy is 0.35eV, and that of the emission energy is 0.25eV. Final 2D maps were achieved via a multi-step data processing including normalization to beam flux and collecting time, integration and combination, etc., which has been elaborated in the previous work (*44*).

Mn-*L* *inverse* partial fluorescence yield (iPFY). Mn-*L* iPFY was achieved through the formula iPFY = *a*/PFY_O, where *a* is a normalization coefficient, PFY_O is extracted by integrating the

fluorescence intensity within the O-*K* emission energy range (495 to 510 eV) on the Mn-*L* mRIXS (white square in Fig. 2B). Quantitative fitting of Mn-*L* iPFY was performed via linear combination with the standard experimental spectra of $Mn^{2+/3+/4+}$, as demonstrated and detailed before (*26*).

O-*K* *super* partial fluorescence yield (sPFY). O-*K* sPFY was achieved by integrating the mRIXS intensity within the emission energy range of 523 to 524.5 eV (between dotted lines in Fig. 3A), where the oxidized oxygen feature emerges. For quantification of the oxidized oxygen feature, the area of the relevant sPFY feature was calculated by integrating the intensity from 530 to 532 eV (shaded area in Fig. 3B, 3C), with a unitized 529.6 eV peak. The “Area Change” in Table 2 is the difference on the integrated sPFY values between the charged and discharged states at a particular cycle.

H2: Supplementary Materials

References and Notes

1. M. Armand, J. M. Tarascon, Building better batteries. *Nature* **451**, 652-657 (2008).
2. J. B. Goodenough, Y. Kim, Challenges for Rechargeable Li Batteries. *Chemistry of Materials* **22**, 587-603 (2010).
3. J. B. Goodenough, K.-S. Park, The Li-ion rechargeable battery: a perspective. *Journal of the American Chemical Society* **135**, 1167-1176 (2013).
4. A. Grimaud, W. T. Hong, Y. Shao-Horn, J. M. Tarascon, Anionic redox processes for electrochemical devices. *Nat Mater* **15**, 121-126 (2016).
5. G. Assat, J.-M. Tarascon, Fundamental understanding and practical challenges of anionic redox activity in Li-ion batteries. *Nature Energy* **3**, 373-386 (2018).
6. X. Rong *et al.*, Anionic Redox Reaction-Induced High-Capacity and Low-Strain Cathode with Suppressed Phase Transition. *Joule* **3**, 1-15 (2018).
7. E. Hu *et al.*, Evolution of redox couples in Li- and Mn-rich cathode materials and mitigation of voltage fade by reducing oxygen release. *Nature Energy* **3**, 690-698 (2018).
8. A. Singer *et al.*, Nucleation of dislocations and their dynamics in layered oxide cathode materials during battery charging. *Nature Energy* **3**, 641-647 (2018).
9. W. Yang, Oxygen release and oxygen redox. *Nature Energy* **3**, 619-620 (2018).
10. S. E. Renfrew, B. D. McCloskey, Residual Lithium Carbonate Predominantly Accounts for First Cycle CO2 and CO Outgassing of Li-Stoichiometric and Li-Rich Layered Transition-Metal Oxides. *J Am Chem Soc* **139**, 17853-17860 (2017).
11. T. Hatsukade, A. Schiele, P. Hartmann, T. Brezesinski, J. Janek, Origin of Carbon Dioxide Evolved during Cycling of Nickel-Rich Layered NCM Cathodes. *ACS Appl Mater Interfaces* **10**, 38892-38899 (2018).
12. T. Teufl, B. Strehle, P. Müller, H. A. Gasteiger, M. A. Mendez, Oxygen Release and Surface Degradation of Li- and Mn-Rich Layered Oxides in Variation of the Li2MnO3 Content. *Journal of The Electrochemical Society* **165**, A2718-A2731 (2018).
13. A. R. Armstrong *et al.*, Demonstrating Oxygen Loss and Associated Structural Reorganization in the Lithium Battery Cathode Li[Ni0.2Li0.2Mn0.6]O2. *Journal of the American Chemical Society* **128**, 8694-8698 (2006).
14. J. Hong *et al.*, Critical Role of Oxygen Evolved from Layered Li–Excess Metal Oxides in Lithium Rechargeable Batteries. *Chemistry of Materials* **24**, 2692-2697 (2012).
15. R. A. House *et al.*, What Triggers Oxygen Loss in Oxygen Redox Cathode Materials? *Chemistry of Materials* **31**, 3293-3300 (2019).
16. R. Jung, M. Metzger, F. Maglia, C. Stinner, H. A. Gasteiger, Oxygen Release and Its Effect on the Cycling Stability of LiNixMnyCozO2 (NMC) Cathode Materials for Li-Ion Batteries. *Journal of The Electrochemical Society* **164**, A1361-A1377 (2017).

17. J. Wandt, A. T. S. Freiberg, A. Ogrodnik, H. A. Gasteiger, Singlet oxygen evolution from layered transition metal oxide cathode materials and its implications for lithium-ion batteries. *Materials Today* **21**, 825-833 (2018).
18. W. Yang, T. P. Devereaux, Anionic and cationic redox and interfaces in batteries: Advances from soft X-ray absorption spectroscopy to resonant inelastic scattering. *Journal of Power Sources* **389**, 188-197 (2018).
19. G. Assat *et al.*, Fundamental interplay between anionic/cationic redox governing the kinetics and thermodynamics of lithium-rich cathodes. *Nat Commun* **8**, 2219 (2017).
20. G. Assat, A. Iadecola, C. Delacourt, R. Dedryvère, J.-M. Tarascon, Decoupling Cationic–Anionic Redox Processes in a Model Li-Rich Cathode via Operando X-ray Absorption Spectroscopy. *Chemistry of Materials* **29**, 9714-9724 (2017).
21. G. Assat, A. Iadecola, D. Foix, R. Dedryvère, J.-M. Tarascon, Direct Quantification of Anionic Redox over Long Cycling of Li-Rich NMC via Hard X-ray Photoemission Spectroscopy. *ACS Energy Letters* **3**, 2721-2728 (2018).
22. K. Dai *et al.*, High Reversibility of Lattice Oxygen Redox Quantified by Direct Bulk Probes of Both Anionic and Cationic Redox Reactions. *Joule* **3**, doi: 10.1016/j.joule.2018.1011.1014 (2018).
23. U. Maitra *et al.*, Oxygen redox chemistry without excess alkali-metal ions in Na2/3[Mg0.28Mn0.72]O2. *Nat Chem* **10**, 288-295 (2018).
24. R. Qiao *et al.*, High-efficiency in situ resonant inelastic x-ray scattering (iRIXS) endstation at the Advanced Light Source. *Review of Scientific Instruments* **88**, 033106 (2017).
25. F. Lin *et al.*, Synchrotron X-ray Analytical Techniques for Studying Materials Electrochemistry in Rechargeable Batteries. *Chemical Reviews*, (2017).
26. Q. Li *et al.*, Quantitative probe of the transition metal redox in battery electrodes through soft x-ray absorption spectroscopy. *Journal of Physics D: Applied Physics* **49**, 413003 (2016).
27. W. E. Gent *et al.*, Coupling between oxygen redox and cation migration explains unusual electrochemistry in lithium-rich layered oxides. *Nat Commun* **8**, 2091 (2017).
28. J. Xu *et al.*, Elucidating anionic oxygen activity in lithium-rich layered oxides. *Nature Communications* **9**, 947 (2018).
29. Z. Zhuo *et al.*, Spectroscopic Signature of Oxidized Oxygen States in Peroxides. *J Phys Chem Lett*, 6378-6384 (2018).
30. S. M. Butorin, J. Guo, N. Wassdahl, E. J. Nordgren, Tunable-excitation soft X-ray fluorescence spectroscopy of high-Tc superconductors: an inequivalent-site seeing story. *Journal of Electron Spectroscopy and Related PhenomenaSpectroscopy of Energy Materials* **110-111**, 235-273 (2000).
31. Z. W. Lebens-Higgins *et al.*, Distinction between Intrinsic and X-ray-Induced Oxidized Oxygen States in Li-Rich 3d Layered Oxides and LiAlO2. *The Journal of Physical Chemistry C* **123**, 13201-13207 (2019).

32. X. Rong *et al.*, Structure-Induced Reversible Anionic Redox Activity in Na Layered Oxide Cathode. *Joule* **2**, 125-140 (2018).
33. K. Du *et al.*, Exploring reversible oxidation of oxygen in a manganese oxide. *Energy & Environmental Science* **9**, 2575-2577 (2016).
34. N. Yabuuchi *et al.*, New O2/P2-type Li-Excess Layered Manganese Oxides as Promising Multi-Functional Electrode Materials for Rechargeable Li/Na Batteries. *Advanced Energy Materials* **4**, 1301453 (2014).
35. N. Yabuuchi *et al.*, A new electrode material for rechargeable sodium batteries: P2-type Na2/3[Mg0.28Mn0.72]O2 with anomalously high reversible capacity. *J. Mater. Chem. A* **2**, 16851-16855 (2014).
36. N. Yabuuchi, Solid-state Redox Reaction of Oxide Ions for Rechargeable Batteries. *Chemistry Letters* **46**, 412-422 (2016).
37. R. Qiao *et al.*, Revealing and suppressing surface Mn(II) formation of Na0.44MnO2 electrodes for Na-ion batteries. *Nano Energy* **16**, 186-195 (2015).
38. W. Yang *et al.*, Key electronic states in lithium battery materials probed by soft X-ray spectroscopy. *Journal of Electron Spectroscopy and Related PhenomenaSpectroscopy of Energy Materials* **190, Part A**, 64-74 (2013).
39. A. J. Achkar *et al.*, Bulk sensitive x-ray absorption spectroscopy free of self-absorption effects. *Physical Review B* **83**, 081106 (2011).
40. R. Qiao, T. Chin, S. J. Harris, S. Yan, W. Yang, Spectroscopic fingerprints of valence and spin states in manganese oxides and fluorides. *Current Applied Physics* **13**, 544-548 (2013).
41. R. Qiao *et al.*, Direct evidence of gradient Mn(II) evolution at charged states in LiNi0.5Mn1.5O4 electrodes with capacity fading. *Journal of Power Sources* **273**, 1120-1126 (2015).
42. J. Xu *et al.*, Elucidating anionic oxygen activity in lithium-rich layered oxides. *Nat Commun* **9**, 947 (2018).
43. B. Song *et al.*, A novel P3-type Na2/3Mg1/3Mn2/3O2 as high capacity sodium-ion cathode using reversible oxygen redox. *Journal of Materials Chemistry A*, (2019).
44. J. Wu *et al.*, Elemental-sensitive Detection of the Chemistry in Batteries through Soft X-ray Absorption Spectroscopy and Resonant Inelastic X-ray Scattering. *Journal of Visualized Experiments*, e57415 (2018).
45. Y. D. Chuang *et al.*, Modular soft x-ray spectrometer for applications in energy sciences and quantum materials. *Rev Sci Instrum* **88**, 013110 (2017).

Acknowledgments

Funding: The Advanced Light Source is supported by the Director, Office of Science, Office of Basic Energy Sciences, of the U.S. Department of Energy under Contract No. DE-AC02-05CH11231. Works at Stanford are supported by the Department of Energy, Office of Science, Basic Energy Sciences, Materials Sciences and Engineering Division, under Contract DE-AC02-76SF00515. Works at Berkeley are partially supported by the Energy Biosciences Institute through the EBI-Shell program. Works at Tsinghua are partially supported by China's National Key R&D Programmes (2018YFB0905105). Some spectroscopic analysis works are supported as part of the NorthEast Center for Chemical Energy Storage (NECCES), an Energy Frontier Research Center funded by Office of Science, Basic Energy Sciences, of the U.S. Department of Energy under Award No. DE-SC0012583. J.W. would like to thank the financial support of the ALS postdoctoral fellowship. The authors thank Yongsheng Hu (IOP) and Xiqian Yu (IOP) for providing the NLMO samples.

Author contributions: W.Y. and J.W. conceived the project and coordinated collaborations with Z.S., R.Z., and Q.L. for contributions from all authors. X.R. and Q.L. synthesized the NLMO materials and conducted electrochemical tests. K.D. and G.L. synthesized NMMO materials and conducted electrochemical tests. J.W., Z.Z., K.D., S.S. and W.Y. performed spectroscopic measurements and analyzed the results. J.W. and W.Y. wrote the manuscript with all authors reviewed and contributed to the discussions.

Competing Interests: The authors declare that they have no competing interests.

Data and materials availability: All data needed to evaluate the conclusions in the paper are present in the paper and/or the Supplementary Materials. Additional data related to this paper may be requested from the authors.

Figures and Tables

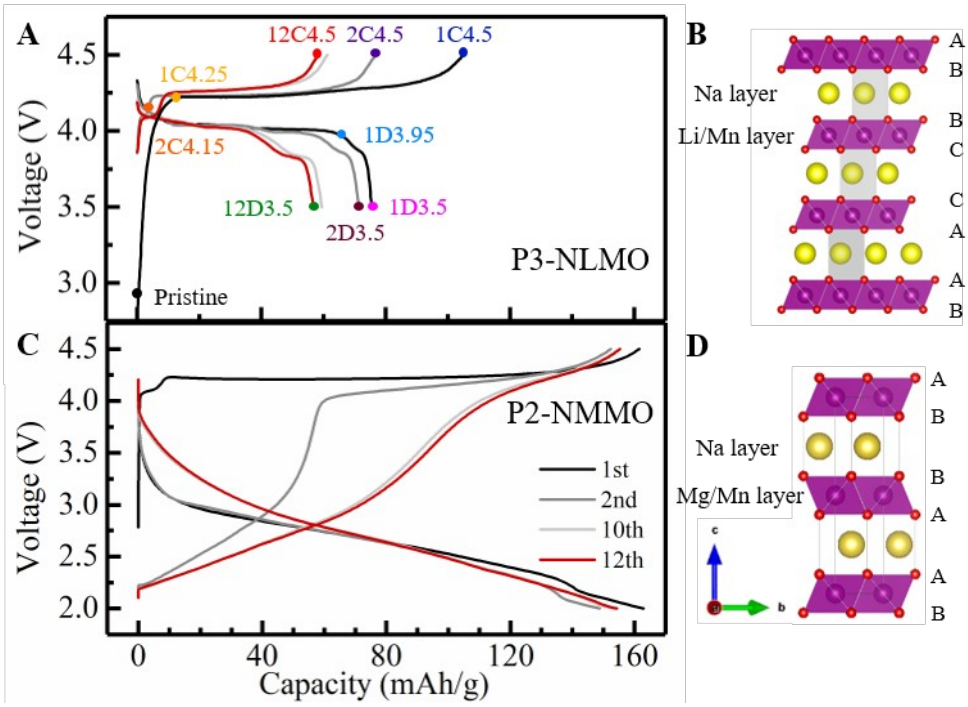

Fig. 1. Contrast between NLMO and NMMO system on capacity and voltage drops. (**A**) Electrochemical profile of NLMO/Na, 3.5 to 4.5V, 0.1C (10 mA g^{-1}). 10 presentative samples with different SOCs from multiple cycles were selected in this study. (**B**) P3-type layered structure of NLMO. (**C**) Electrochemical profile of NMMO/Na, 2.0 to 4.5V, 0.1C. (**D**) P2-type layered structure of NMMO with a different stacking.

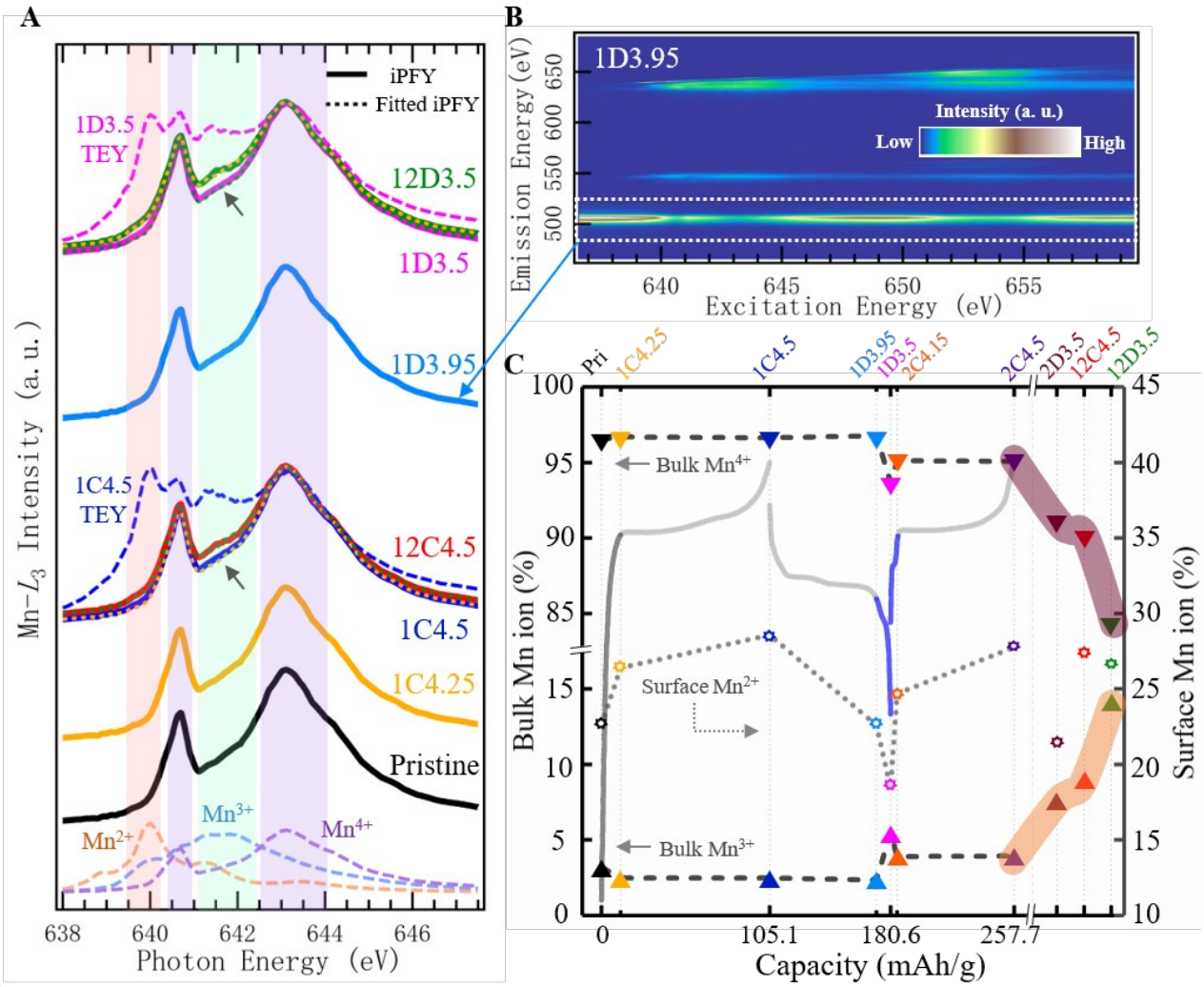

Fig. 2. Quantification of bulk and surface Mn oxidation states upon cycling. (**A**) Mn-L_3 mRIXS-iPFY spectra as bulk probes (solid lines) and two typical TEY spectra of 1C4.5 and 1D3.5 as surface probes (dashed lines) of the Mn states. The mRIXS-iPFY are fitted precisely (dotted lines) via linear combination of the $Mn^{2+/3+/4+}$ reference spectra (dashed lines at bottom), with the fitting results of all samples in Table 1. Data from the 12th cycle fully charged (12C4.5) and discharged (12D3.5) electrodes are plotted with the 1st cycle data for direct comparison. Difference between the 1st and 12th cycle (grey arrows) indicates the accumulation of Mn^{3+} upon cycling. (**B**) A typical Mn-*L* mRIXS collected from 1D3.95 sample. The white frame indicates the area where iPFY is extracted by the inversed integration of the signals (see Methods). (**C**) The bulk Mn valence contents (left axis, triangles) and surface Mn^{2+} contents (right axis, circles) obtained through the quantitative fittings of the mRIXS-iPFY and sXAS-TEY spectra, respectively. Data are plotted upon cycling capacity with cycling profile over-plotted. Other than the representative results shown here, the sXAS, mRIXS, and mRIXS-iPFY (with fittings) of all samples are presented in Fig. S4, S5, and S6, respectively.

920

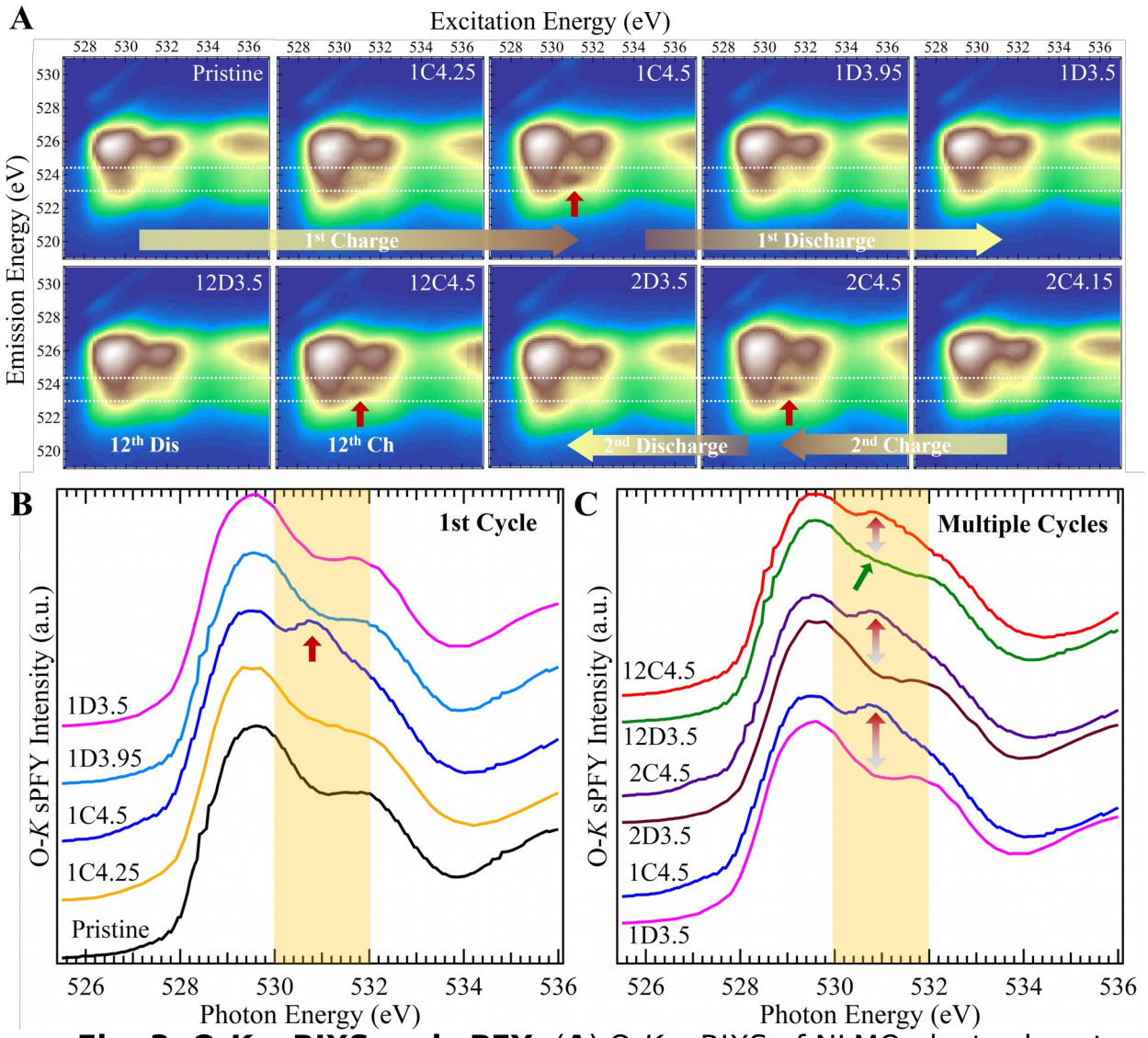

Fig. 3. O-*K* mRIXS and sPFY. (**A**) O-*K* mRIXS of NLMO electrodes at different electrochemical states. Red arrows indicate the oxidized oxygen feature at charged states, representing the lattice OR reactions (see text). Dotted lines on mRIXS images indicate the energy range for extracting sPFY spectra (see Methods). (**B**) O-*K* mRIXS-sPFY of 1st cycle, with area changes between 530-532 eV (shaded area) upon electrochemical cycling. (**C**) O-*K* mRIXS-sPFY of multiple cycles. The lattice OR contribution is reflected by the sPFY intensity difference within the shaded area between the charged and discharged electrodes, as indicated by double-arrows. Green arrow points to an obviously enhanced area at the 12th discharge, compared with the discharged states in the 1st and 2nd cycles.

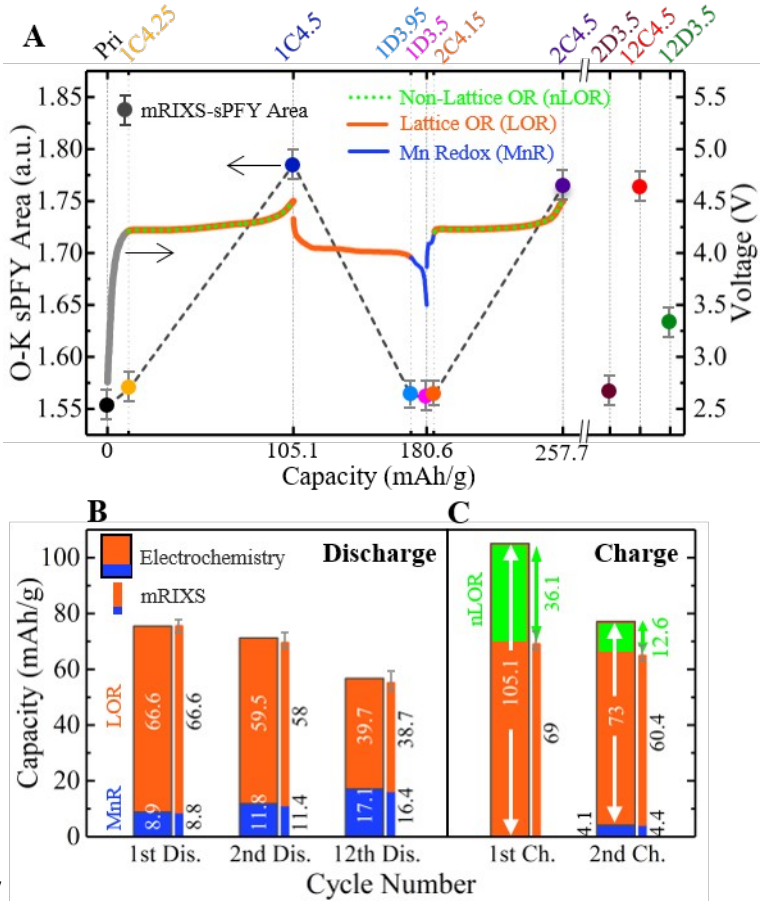

Fig. 4. Summary of quantification values of three different redox reactions in NLMO. (**A**) The O-*K* mRIXS-sPFY peak area (dots and dashed lines, left axis) is plotted together with the cycling profile (right axis). Variations in sPFY peak area indicates the amount of lattice OR (LOR) reactions. Cycling profile is colored to show the three different kind of redox reactions at different voltage range, with red, blue and green (dotted) representing lattice OR, Mn, and non-lattice OR reactions, respectively. Note the range for Mn OR is also defined experimentally in Fig. 2C. (**B**) Two sets of capacity contributions of Mn redox (MnR, blue) and lattice O redox (LOR, red) during the 1st, 2nd and 12th discharge. Values of the framed wide columns are directly electrochemical capacities but with the lattice OR and Mn redox boundaries defined by mRIXS results (Fig. 2C, 4A). Capacity contribution values from "mRIXS" are calculated based on spectroscopic results themselves. Mn redox contribution is calculated based on the quantified Mn valence states (Table 1). Lattice OR contribution is quantified by the mRIXS-sPFY intensity change between charged and discharged states (Fig. 3C) with a conversion ratio (see text). The consistence between electrochemistry and mRIXS results validates that lattice OR dominates the discharging processes. (**C**) Two sets of capacity contributions of Mn redox (MnR, blue) and lattice O redox (LOR, red) during charging quantified through the same two methods

based on electrochemical capacity and mRIXS results. Unlike the discharged states, the quantified LOR capacity from mRIXS is dramatically smaller than the total OR capacity in electrochemistry (white double arrows), indicating a large amount of non-lattice oxygen redox (nLOR) during charge (green).

Table 1. Contents of Mn valence states in bulk and on surface.

Quantification values are based on fitting the Mn-*L* mRIXS-iPFY (for bulk) and sXAS-TEY (for surface) spectra. Capacity contribution of Mn redox (MnR) is then calculated directly based on the bulk Mn valence state changes. (Fitting results with standard deviations are in Table S1 & S2.) Additionally, Mn capacity contribution from electrochemistry is obtained by extracting the capacity of the cycling profile in the range with Mn-*L* spectral changes (Fig. 2C).

	Surface Mn^{2+} (%)	Bulk Mn^{3+} (%)	Bulk Mn^{4+} (%)		Mn charge transfer (mol)	Mn capacity contribution by mRIXS (mA·h/g)	Mn capacity contribution from electrochemistry (mA·h/g)
Pristine	22.58	3.21	96.53				
1C4.25	26.38	2.48	96.69	**1st Charging**	≈ 0.001	< 0.01	—
1C4.5	28.57	2.48	96.64				
1D3.95	22.58	2.34	96.77	**1st Discharging**	0.030	8.8	8.9
1D3.5	18.44	5.51	93.67				
2C4.15	24.68	3.89	95.11	**2nd charging**	0.015	4.4	4.1
2C4.5	27.78	3.94	95.08				
2D3.5	21.62	7.83	91.16	**2nd discharging**	0.039	11.4	11.8
12C4.5	27.47	9.03	90.28				
12D3.5	26.49	14.62	84.62	**12th discharging**	0.056	16.4	17.1

Table 2. Lattice and total OR capacities quantified through both electrochemical profile and mRIXS-sPFY area changes. Changes of "O-K mRIXS-sPFY area" indicates the amount of lattice OR (Fig. 3C). Capacity contributions of lattice OR (LOR) is calculated based on sPFY area change with a conversion ratio of 303 mAh/g per area change (see text). The discharge process is dominated by LOR activities, however, LOR capacity during charge is much lower than the electrochemical capacities, indicating a significant amount of non-lattice oxygen redox (nLOR) during charge.

	O-*K* mRIXS-sPFY area (a.u.)	Std. Dev.		Area change (a.u.)	LOR capacity by mRIXS (mA·h/g)	Total OR capacity from electrochemistry (mA·h/g)	Ratio
Pristine	1.553	0.040					
1C4.25	1.599	0.065	**1st Charging**	0.232	69.0	105.1	65.7%
1C4.5	1.785	0.052					
1D3.95	1.565	0.046	**1st Discharging**	0.224	Benchmark: 66.6 (Capacity/Area = 66.6/0.224)		100%
1D3.5	1.561	0.057					
2C4.15	1.571	0.055	**2nd charging**	0.203	60.4	73.0	82.7%
2C4.5	1.764	0.052					
2D3.5	1.569	0.046	**2nd discharging**	0.195	58.0	59.5	97.5%
12C4.5	1.763	0.052					
12D3.5	1.633	0.064	**12th discharging**	0.130	38.7	39.7	97.5%